Biomimetic model to reconstitute angiogenic sprouting morphogenesis in vitro

Duc-Huy T. Nguyen[a,1], Sarah C. Stapleton[a,1], Michael T. Yang[b], Susie S. Cha[b], Colin K. Choi[b], Peter A. Galie[b], and Christopher S. Chen[a,b,2]

Departments of [a]Chemical and Biomolecular Engineering and [b]Bioengineering, University of Pennsylvania, Philadelphia, PA 19104

Edited by David A. Tirrell, California Institute of Technology, Pasadena, CA, and approved March 15, 2013 (received for review December 10, 2012)

Angiogenesis is a complex morphogenetic process whereby endothelial cells from existing vessels invade as multicellular sprouts to form new vessels. Here, we have engineered a unique organotypic model of angiogenic sprouting and neovessel formation that originates from preformed artificial vessels fully encapsulated within a 3D extracellular matrix. Using this model, we screened the effects of angiogenic factors and identified two distinct cocktails that promoted robust multicellular endothelial sprouting. The angiogenic sprouts in our system exhibited hallmark structural features of in vivo angiogenesis, including directed invasion of leading cells that developed filopodia-like protrusions characteristic of tip cells, following stalk cells exhibiting apical–basal polarity, and lumens and branches connecting back to the parent vessels. Ultimately, sprouts bridged between preformed channels and formed perfusable neovessels. Using this model, we investigated the effects of angiogenic inhibitors on sprouting morphogenesis. Interestingly, the ability of VEGF receptor 2 inhibition to antagonize filopodia formation in tip cells was context-dependent, suggesting a mechanism by which vessels might be able to toggle between VEGF-dependent and VEGF-independent modes of angiogenesis. Like VEGF, sphingosine-1-phosphate also seemed to exert its proangiogenic effects by stimulating directional filopodial extension, whereas matrix metalloproteinase inhibitors prevented sprout extension but had no impact on filopodial formation. Together, these results demonstrate an in vitro 3D biomimetic model that reconstitutes the morphogenetic steps of angiogenic sprouting and highlight the potential utility of the model to elucidate the molecular mechanisms that coordinate the complex series of events involved in neovascularization.

3D culture | microfabrication | microfluidics | gradient | fluid flow

Angiogenesis, the process by which new capillary vessels sprout from existing vasculature, plays a critical role in embryonic development and wound healing, and its dysregulation can contribute to cancer progression as well as numerous inflammatory and ischemic diseases (1, 2). Consequently, therapeutic strategies to suppress, enhance, or normalize angiogenesis are widely sought to treat a broad spectrum of diseases (1, 2). The most mature among these approaches targets the activity of angiogenic growth factors, such as vascular endothelial growth factor (VEGF), to modulate relevant signaling pathways and control the angiogenesis process. Indeed, inhibitors of such pathways have emerged as a mainstay therapy for some cancers and diabetic retinopathy (3–5). However, it is still unclear how the endothelial cells (ECs) lining blood vessels form new vessels, or how angiogenic factors regulate such a dynamic, multicellular process.

Examining the physical process of angiogenesis requires experimental systems in which the formation of new capillary vessels can be easily observed and manipulated. Commonly used in vivo models such as the mouse dorsal window chamber, chick chorioallantoic membrane, and mouse corneal micropocket assays provide important validation platforms (6, 7) but are low-throughput and less suitable for identifying new cell biological mechanisms. In contrast, many traditional cell culture models of angiogenesis bear little anatomical resemblance to the in vivo process. For instance, the tube formation assay involves the reorganization of ECs seeded onto the surface of Matrigel into multicellular cords that partially resemble vascular networks but lack important features observed in native angiogenesis, such as directional invasion of cells into a 3D extracellular matrix (ECM), proper polarization of the luminal and abluminal sides of ECs, lumen formation, and support of fluid flow (6, 8). In contrast, collagen- and fibrin-based tubulogenesis (9), bead sprouting assays (10), and aortic ring explants (11) have provided valuable experimental models that better recapitulate aspects of sprouting and lumenization, but these models still lack the continuous flow known to fundamentally affect endothelial cell behavior (6, 12).

Organotypic models that have faithfully captured biological structure and the biophysical environment have proven to be transformative for a field, as exemplified by studies of engineered skin or mammary epithelial morphogenesis (13–15). Here, we demonstrate the use of endothelium-lined channels as a platform to recapitulate angiogenic sprouting in vitro. The system allowed us to screen combinations of angiogenic factors and identify cocktails that induced highly organized, directed multicellular sprouting into a surrounding ECM that seems to mimic key morphological aspects of in vivo angiogenesis not yet described by other in vitro models. Furthermore, we demonstrate the utility of this model by illustrating how pro- and antiangiogenic agents affect the complex multicellular process of angiogenesis.

Results

Microengineered Platform That Supports Angiogenic Sprouting and Neovessel Formation in Vitro. To study the process of angiogenic invasion and sprouting from an existing vessel, we designed a device in which an endothelium lining a cylindrical channel was fully surrounded by matrix and exposed to a gradient of angiogenic factors emanating from a parallel source channel (Fig. 1*A*). The device was assembled by casting type-I collagen into a poly (dimethylsiloxane) (PDMS) mold/gasket with two parallel needles held across the casting chamber. Upon collagen polymerization, the needles were extracted to create hollow cylindrical channels in the collagen matrix (Fig. 1*A*). ECs were then injected into one of the channels, allowing them to attach on the interior wall and form a confluent endothelium or "parent vessel" (Fig. 1*B*). Flow was maintained through both channels for the duration of the experiments and media containing angiogenic factors was subsequently added to the second channel to establish a gradient across the collagen matrix to the endothelium (Fig. S1). Thus,

Author contributions: D.-H.T.N., S.C.S., and C.S.C. designed research; D.-H.T.N., S.C.S., M.T.Y., S.S.C., and P.A.G. performed research; M.T.Y. contributed new reagents/analytic tools; D.-H.T.N., S.C.S., and P.A.G. analyzed data; and D.-H.T.N., S.C.S., M.T.Y., C.K.C., and C.S.C. wrote the paper.

The authors declare no conflict of interest.

This article is a PNAS Direct Submission.

[1]D.-H.T.N. and S.C.S. contributed equally to this work.

[2]To whom correspondence should be addressed. E-mail: chrischen@seas.upenn.edu.

This article contains supporting information online at www.pnas.org/lookup/suppl/doi:10.1073/pnas.1221526110/-/DCSupplemental.

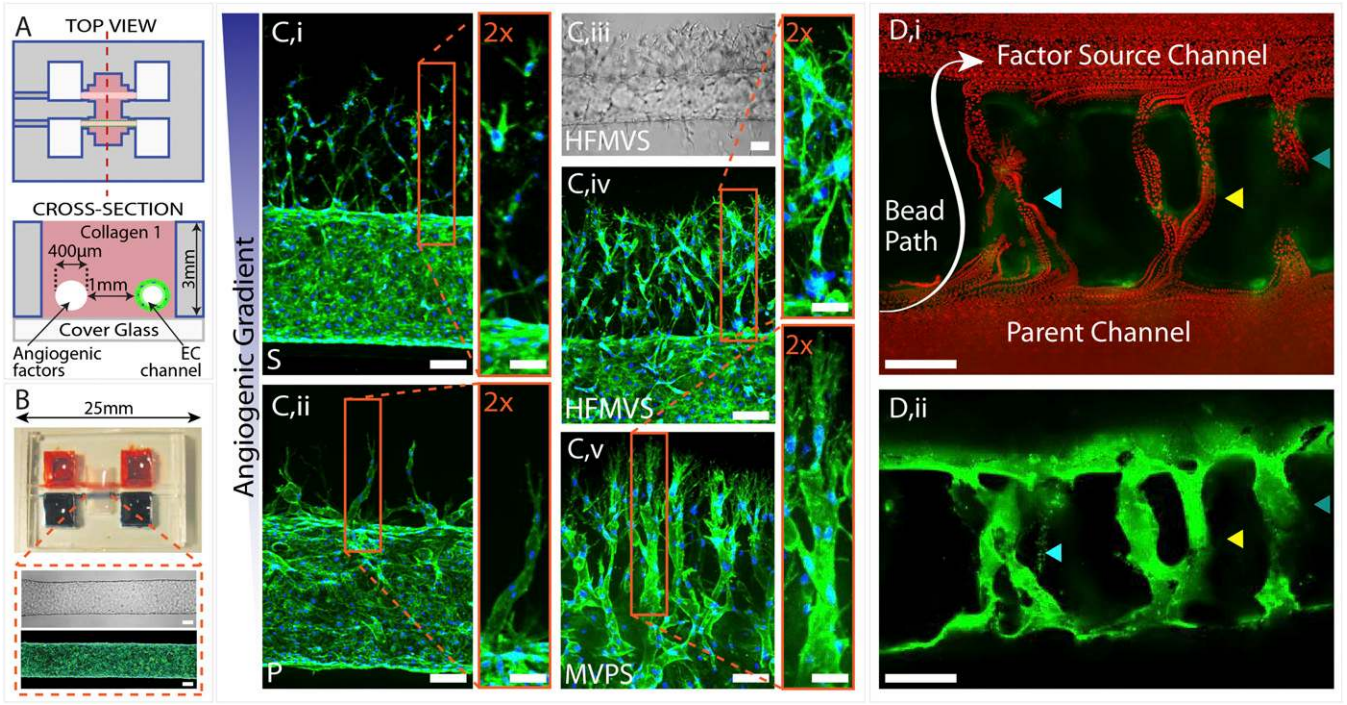

Fig. 1. Three-dimensional formation of endothelial sprouts and neovessels in a microfluidic device. (*A*) Device schematic. Parallel cylindrical channels are encased in a 3D collagen matrix within a microfabricated PDMS gasket and connected to fluid reservoirs. One channel is coated with ECs and perfused with medium and the other channel is perfused with medium enriched with angiogenic factors. (*B*) Photograph of the device. Zoom shows phase (*Upper*) and fluorescent (*Lower*) micrographs of an endothelialized channel. F-actin and nuclei are labeled with phalloidin (green) and DAPI (blue), respectively. (*C*) Representative confocal immunofluorescence images of sprouting and migrating ECs in response to gradients of different proangiogenic factors: S (*i*), P (*ii*), HFMVS cocktail (*iv*), and MVPS cocktail (*v*); *iii* shows a phase image of directed sprouting induced by HFMVS. F-actin and nuclei are labeled with phalloidin (green) and DAPI (blue), respectively. (*D*) Neovessels in the device are shown in (*i*) a merged image of a time-lapse movie tracking the position of 3-μm red fluorescent beads perfused through the large channels and neovessels and (*ii*) a z-projection confocal image of the same vessels. Beads were added to the left end of the parent vessel and flowed through neovessels to the factor source channel. In both images ECs (green) are labeled with DiI. F, bFGF; H, HGF; M, MCP-1; P, PMA; S, S1P; V, VEGF. (Scale bars: 2× zoom-in *Insets* in *C*, 50 μm; all other scale bars, 100 μm.)

the device design provided a means to promote and visualize endothelial sprouting that might emulate early angiogenic processes.

Using this device, we first examined how various proangiogenic factors might affect directed invasion and sprouting from the parent vessel. Six common factors associated with angiogenesis in the literature were selected: basic fibroblast growth factor (bFGF) (16), hepatocyte growth factor (HGF) (17), VEGF (18, 19), monocyte chemotactic protein-1 (MCP-1) (20), sphingosine-1-phosphate (S1P) (21, 22), and phorbol 12-myristate 13-acetate (PMA) (23). After these factors were added individually to the nonendothelialized source channel, phase-contrast and confocal microscopy were used to assess the organization and development of EC invasion over 4 d. We found that VEGF, MCP-1, HGF, or bFGF alone did not induce significant invasion into the matrix, whereas S1P and PMA resulted in substantial directed invasion (Fig. S2). This invasion was oriented directly toward the source channel, despite the fact that cell migration from the endothelium was not artificially constrained in any direction by our system design (Fig. 1*C*).

Interestingly, S1P and PMA stimulated markedly different modes of cell migration. S1P drove chemotactic migration primarily of single cells from the endothelialized channel, whereas PMA triggered collective cell migration that manifested itself in the form of sparse, long, multicellular sprouts into the matrix (Fig. 1 *C*, *i* and *ii*). Progressively more complex combinations of the six factors yielded more substantial multicellular sprout-like structures, especially in the case of two distinct combinations that drove robust sprouting: HGF, bFGF, MCP-1, VEGF, and S1P (HFMVS); and MCP-1, VEGF, PMA, and S1P (MVPS) (Fig. S2). HFMVS-guided invasion exhibited numerous sprout-like structures that extended hundreds of micrometers from the endothelialized parent vessel as well as large numbers of solitary cells migrating into the matrix (Fig. 1*C*, *iii* and *iv*). The MVPS cocktail induced an even greater multicellular sprouting response with less single cell migration (Fig. 1*C*, *v*). In both cases, the sprouts continued to invade toward the source channel as long as the gradient was maintained.

Remarkably, when the tips of these sprouts reached the source channel (typically after 1 wk), they breached into the source channel, forming what seemed to be new microvessels connecting the two parallel channels (Fig. 1*D*). To test whether these "neovessels" possessed functional, perfusable lumens, 3-μm fluorescent beads were added to the media flowing into the endothelialized parent channel. Beads traveled through the neovessels to the source channel with no leakage into the interstitial space, indicating fully developed lumens lined by a continuous endothelium. Overlaying frames of the time-lapse images demonstrated the path of the beads through these occasionally branching neovessels (Fig. 1*D* and Movie S1).

Sprouts Exhibit Morphologic Features of in Vivo Angiogenesis. Because this experimental model allows us to monitor the detailed structural events of sprouting, we next proceeded to examine the changes in cellular organization during early stages of invasion. For this purpose, we focused on the MVPS cocktail, which promoted the greatest sprouting response with minimal single-cell migration. Before stimulation, cells in the endothelialized channel exhibited the expected apical–basal polarity as demonstrated by the localization of the CD34 apical marker podocalyxin to the luminal face (24). On the basolateral side of the endothelium we observed both laminin and collagen IV deposition, suggestive of

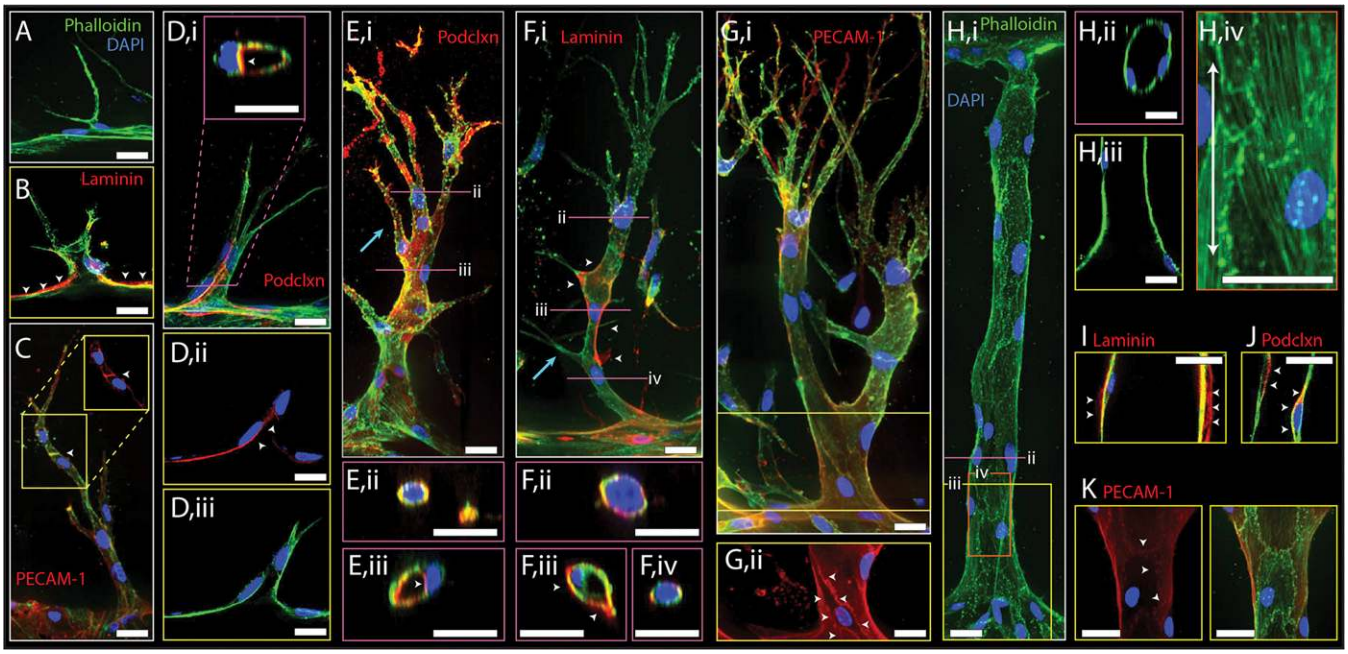

Fig. 2. Characterization of early and late sprouts and neovessels. Representative confocal immunofluorescence images of early (*A–D*) and late (*E–G*) sprouts and neovessels (*H–K*). For all images F-actin and nuclei are labeled with phalloidin (green) and DAPI (blue), respectively. Staining for laminin (*B*, *F*, and *I*), PECAM-1 (*C*, *G*, and *K*), and podocalyxin (podclxn; *D*, *E*, and *J*) are shown in red. (*A*) Micrograph of an EC extending processes into the matrix toward the source channel. (*B*) Laminin immunofluorescence (red) is marked by white arrowheads on the abluminal side of the parent vessel. Fluorescence is interrupted by early sprout invasion. (*C*) Image of an early multicellular sprout stained for F-actin (green) and PECAM-1 (red). White arrowheads point to PECAM-1 staining at cell–cell junctions. (*Inset*) Z-projection of back half of sprout showing only red channel (PECAM-1). (*D*) Early sprout stained for podocalyxin (red) shown in z-projection (*i*) and single slice (*ii* and *iii*). White arrowheads mark podocalyxin at luminal side of sprout shown by transverse (*Inset*, *i*) and in-plane (*ii*) sections. (*E*) Mature sprout stained for podocalyxin (red) shown in z-projection (*i*) with blue arrow marking cell invading out from sprout stalk, in cross-sections of tip cell (*ii*) showing no lumen or spatial podocalyxin localization in the cell, and stalk (*iii*) with white arrowheads marking podocalyxin staining at apical side of lumenized stalk cells. (*F*) Mature sprout stained for laminin (red) shown in z-projection (*i*) with blue arrow marking stalk cell filopodia, and in cross-sections of sprout tip cell (*ii*) that contains no lumen and shows presence of laminin staining, in lumen-containing stalk cell (*iii*) with white arrowheads marking laminin staining at basal side, and stalk cell that contains no lumen (*iv*) showing laminin immunofluorescence. (*G*) Mature sprout stained for PECAM-1 (red) shown in full z-projection (*i*) and z-projection of back half of sprout (*ii*). White arrowheads in (*ii*) mark PECAM-1 staining at cell junctions. (*H*) Neovessel shown in z-projection (*i*), cross-section (*ii*), and in-plane slice (*iii*). F-actin (*iv*) shows actin fiber alignment with direction of flow indicated by double-arrow line. (*I*) Neovessel exhibits laminin staining (red) at its basal side (white arrowheads). (*J*) Neovessel exhibits podocalyxin staining (red) at its luminal side (white arrowheads). (*K*) Neovessels express PECAM-1 staining (red) at cell junctions (white arrowheads). Yellow, pink, and orange boxes indicate longitudinal slice or partial stack, transverse cross-section, and zoom-in, respectively. (Scale bars: 25 μm.)

a cell-deposited matrix layer enveloping the parent vessel (Fig. S3). Upon stimulation, occasional single ECs began invading into the matrix and extending filopodia-like protrusions in the direction of the angiogenic gradient (Fig. 2*A*). During initial invasion, we observed interruptions in laminin immunofluorescence, consistent with focal degradation of the cell-deposited ECM reminiscent of basement membrane (Fig. 2*B*). These leading tip cells were replete with filopodia-like protrusions, morphologically recapitulating in vivo sprout tips (25). As these tip cells migrated deeper into the matrix, neighboring cells followed while maintaining cell–cell contacts along the length of the sprout, as shown by platelet endothelial cell adhesion molecule-1 (PECAM-1) staining (Fig. 2*C*). Thus, the sprouting process from the parent endothelium into the matrix involved collective cell migration that supported a contiguous structure between the sprout and parent vessel. Even at this early stage of two to three cells per sprout, evidence of lumen formation was detected in 3D reconstructions of confocal images (Fig. 2*D*). Moreover, apical–basal polarity seemed intact in the sprout, as evidenced by apically targeted podocalyxin staining (Fig. 2 *D*, *i* and *ii*).

As the sprouts continued to invade and extend into the matrix, they became longer, contained progressively more cells, and began to branch (Fig. 2 *E–G*). Stereotypical sprouting morphology was evident in these mature sprouts, with cells at the sprout tip developing numerous thin filopodia-like protrusions, in contrast to cells in the stalk containing few filopodia protrusions (Fig. 2 *E–G*). Lumens developed in both early and late sprouts that often extended from the parent vessel up to, but never within, the tip cell (Fig. 2 *D* and *E*). Partial lumens occasionally were evident behind the tip cell and were not connected to the parent vessel, suggestive of spontaneous, focal cord-hollowing or lumenization (Fig. 2 *F*, *iv*). Staining confirmed that the sprout tip cells lacked specific localization of podocalyxin, whereas stalk cells demonstrated localization of podocalyxin to the luminal space (Fig. 2*E*). We observed laminin deposition in the mature sprouts (Fig. 2*F*) and found that PECAM-1–positive cell–cell junctions were generally intact throughout the sprouts (Fig. 2*G*). In addition to primary sprouts, maturation of secondary branches also occurred in our system. Different stages of secondary branching were evidenced by stalk cells occasionally marked by direct filopodia-like protrusions suggesting early branch initiation (Fig. 2*F*, blue arrow), whole cells extending out from the stalk of the sprout (Fig. 2*E*, blue arrow), and finally as full multicellular branches with their own new tip cells extending toward the angiogenic gradient (Fig. 2*G*).

Upon formation of neovessels spanning the two channels, nonperfused filopodial protrusions notably disappeared (Fig. 2 *H*, *i*). The neovessels were lumenized end-to-end (Fig. 2 *H*, *ii* and *iii*), and cells were aligned with flow as in the parent vessel, demonstrated by actin stress fiber alignment (Fig. 2 *H*, *iv*). Further examination revealed the deposition of laminin around the neovessels (Fig. 2*I*), localization of podocalyxin to the luminal

domains (Fig. 2*J*), and PECAM-1 staining reflective of intact cell–cell junctions (Fig. 2*K*).

VEGF Drives Directed Filopodia Formation and Sprout Extension in a Context-Dependent Manner. Although the structural similarities between angiogenic sprouts observed in our system and those found in vivo were broadly encouraging, it was also important to explore whether our angiogenic sprouts responded physiologically to agents known to perturb the angiogenic process. To address this question, we investigated whether antiangiogenic agents could affect sprouting in our system. First, a VEGF receptor 2 (VEGFR2) inhibitor, Semaxanib (26, 27), was added with the HFMVS angiogenic cocktail. If added from the outset, the inhibitor abrogated sprout initiation (Fig. 3*A*). Because angiogenic inhibitors are also thought to lead to regression of preexisting sprouts (28), we also tested the effects of adding Semaxanib to the source channel after 3 d of uninhibited sprouting. We found that further progression of sprouts was arrested, but obvious regression of the sprouts did not occur (Fig. 3*A*). Closer inspection of VEGFR2-inhibited sprout architectures revealed a nearly complete loss of the many filopodia-like protrusions normally present in the tip cells, with a decrease in the number of protrusions (Fig. 3 *B* and *C*). The average length of the few remaining protrusions was not significantly different from that of the untreated sprouts. Surprisingly, we observed that sprouting induced by the MVPS cocktail, while slowed, seemed to proceed despite VEGFR2 inhibition (Fig. 3*D*). Confocal images revealed that the filopodia-like protrusions in these sprouts were largely unaffected by Semaxanib, whether added at day 0 or day 3 (Fig. 3*F*). Quantitative analysis showed that the number of filopodial extensions was unchanged and their length was unaffected (Fig. 3*E*). To further test the role of VEGF in the MVPS cocktail, we compared sprouting induced by MPS versus MVPS cocktails (Fig. S4) and indeed found no significant difference between these two cocktails. Importantly, these results demonstrate that the angiogenic process modeled by our system can respond to physiologically relevant antiangiogenic therapeutics. Moreover, this system offers insights into the mechanism by which Semaxanib may antagonize angiogenesis, by arresting the formation of cellular protrusions that are critical to the initiation and growth of angiogenic sprouts. Interestingly, in contexts containing factors that can promote protrusive activity in a VEGF-independent manner, angiogenic sprouts become refractory to Semaxanib.

S1P and Matrix Metalloproteinase Inhibition Demonstrate Independent Steps for Angiogenic Invasion. To further investigate the morphogenetic responses to antiangiogenic factors, we examined the effects of perturbing S1P signaling, which acts as a strong chemoattractant through a G protein-coupled receptor (S1PR) and is known to regulate angiogenesis (22, 29). Exposing cells to the S1PR inhibitor Fingolimod (30) resulted in abrogation of sprout initiation when introduced at day 0 and inhibited further sprout extension when given at day 3 (Fig. 4). Interestingly, these effects were independent of which angiogenic cocktail (HFMVS or MVPS) was used (Fig. 4 *A* and *D*). Quantification of the remaining sprout structures revealed nearly complete loss in the number of filopodia-like protrusions, with cells appearing less elongated and organized (Fig. 4 *B*, *C*, *E*, and *F*). Given the polarizing effects of S1P on filopodia, we used the system to explore whether changing the S1P gradient would affect sprouting. Holding MCP-1, VEGF, and PMA constant in the source channel, we found that sprouting required S1P provided by the source channel, regardless of whether S1P was present in the endothelialized lumen. We also found that, although its presence was necessary, varying the concentration of S1P by half or twofold did not seem to affect the speed of sprout progression (Fig. S5). Together, these data suggest that S1P signaling also regulates angiogenic sprouting, and that multiple pathways in addition to VEGF signaling may contribute specifically to the directional protrusions necessary for sprout extension. However, although necessary, we would anticipate that filopodial protrusions are only one of several key cellular processes required for sprout extension. In support of this, we observed that the broad-spectrum matrix metalloproteinase (MMP) inhibitor Marimastat (31, 32) also blocked sprout invasion and extension (Fig. S6) but had no effect on directed filopodial extension.

Discussion

Although central to angiogenesis, the morphogenetic process of endothelial invasion and sprout extension has been difficult to observe in vivo, and models of sprouting in vitro have largely ignored the key initial conditions in which sprouts emanate from ECs lining a perfused vessel. Several approaches have been developed recently in which endothelial cells seeded into a channel within ECM form a primitive vasculature (33–35). Although they offer an in vitro model of vessel biology, so far these single-compartment microfluidic systems have not demonstrated control over angiogenic sprouting. Here, we built on this concept with a device containing a second channel that introduces angiogenic factors to trigger directed sprouting from the vessels. Other designs have

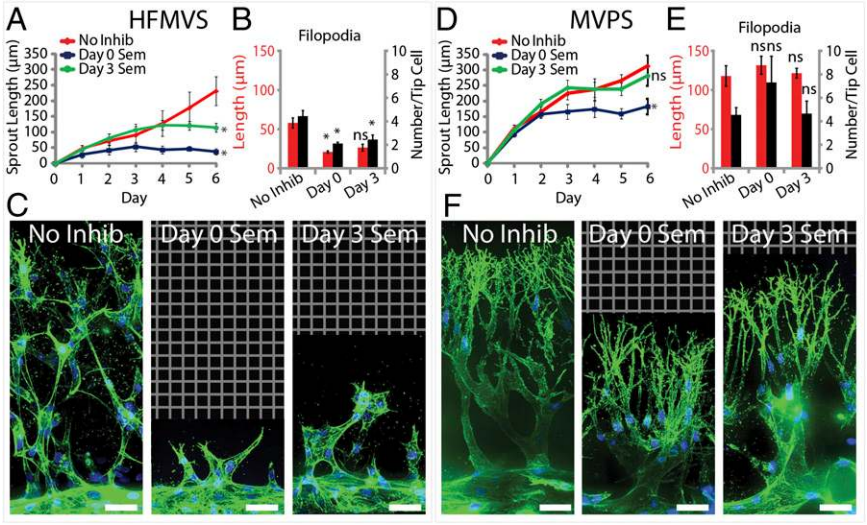

Fig. 3. Effects of VEGFR2 inhibition on angiogenic sprouting. (*A* and *D*) Plot of sprout length driven by HFMVS (*A*) or MVPS (*D*) in response to Semaxanib treatment over time. Proangiogenic cocktail was initiated at day 0 and Semaxanib treatment was initiated at either day 0 (Day 0 Sem), day 3 (Day 3 Sem), or never (No Inhib). (*B* and *E*) Quantification of filopodia length and number in sprouting for inhibitor treatment versus no-inhibitor control. (*C* and *F*) Representative confocal immunofluorescence images of indicated conditions at day 6. F-actin and nuclei are labeled with phalloidin (green) and DAPI (blue), respectively. Grid indicates no detectable signal, so no data were acquired. (Scale bars: 50 μm.) Error bars are SEM. *Significant difference from control ($P < 0.05$); ns, no significant difference from control. $n = 5$ samples for sprout length quantification and $n = 3$ samples for filopodia quantification. All filopodia quantifications performed on data from day 6 of the experiment.

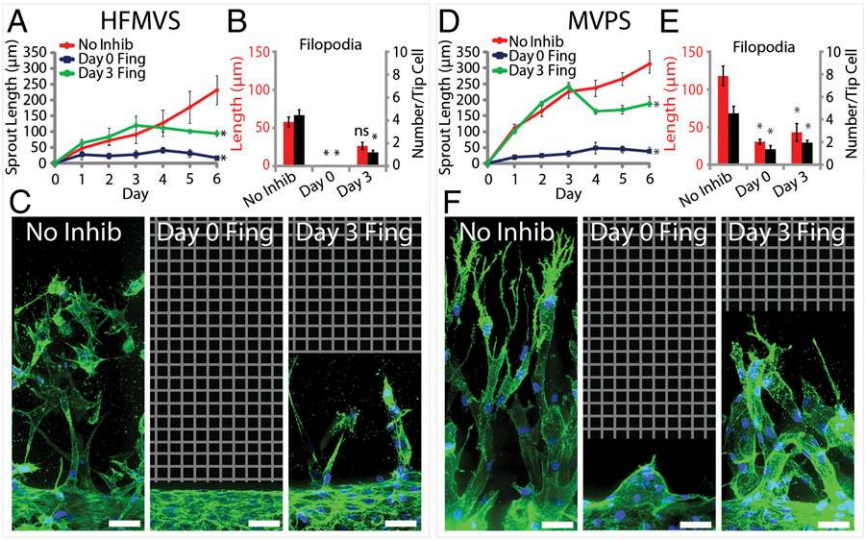

Fig. 4. Effects of S1P receptor inhibition on angiogenic sprouting. (*A* and *D*) Plot of sprout length driven by HFMVS (*A*) or MVPS (*D*) in response to Fingolimod treatment over time. Proangiogenic cocktail was initiated at day 0 and Fingolimod treatment was initiated at either day 0 (Day 0 Fing), day 3 (Day 3 Fing), or never (No Inhib). (*B* and *E*) Quantification of filopodia length and number in sprouting for inhibitor treatment versus no-inhibitor control. (*C* and *F*) Representative confocal immunofluorescence images of indicated conditions at day 6. F-actin and nuclei are labeled with phalloidin (green) and DAPI (blue), respectively. Grid indicates no detectable signal, so no data were acquired. (Scale bars: 50 μm.) Error bars are SEM. *Significant difference from control ($P < 0.05$); ns, no significant difference from control. $n = 5$ samples for sprout length quantification and $n = 3$ samples for filopodia quantification. All filopodia quantifications performed on data from day 6 of the experiment.

been presented for studying sprouting in the presence of flow (36–38). These use microfluidic channels with square rather than circular cross-sections, where three walls are silicone or glass and one sidewall is the edge of an ECM matrix compartment that contains PDMS posts for structural support. Thus, cells are exposed to surfaces other than the ECM itself both at the outset and during invasion, which could affect and constrain cell migration, sprouting geometry, and multicellular organization. As such, the simplicity of such devices make them excellent tools to assay very early sprouting events, but they may not be ideal for observing unconstrained morphogenetic responses. In contrast, the system presented here offers gradient-driven angiogenic sprouting from a fully encapsulated endothelialized channel, thus allowing cells to emanate outward from the vessel wall in all directions without contacting artificial surfaces, and thus provides a unique avenue for studying multicellular, morphogenetic aspects of angiogenesis.

The ability to assess the 3D multicellular organization of invading cells was a critical feature that enabled us to characterize and isolate factors that support the many steps involved in angiogenic sprouting. In our system, VEGF alone had negligible effect on sprouting, whereas S1P only triggered single-cell migration. Instead, only in the presence of a more complex cocktail of multiple factors could we observe robust multicellular sprout-like invasion where a morphologically distinct leading tip cell was trailed by a multicellular stalk. Interestingly, our results suggest that different combinations of factors can be similarly potent. In line with these findings, one study reported a combination of factors secreted by stromal fibroblasts that induced sprouting (39), and another found a combination of hematopoietic chemokines led to a marked enhancement in tubulogenesis and sprouting (40). The recognition that multiple combinations of factors can drive angiogenesis, likely through different mechanisms, further underscores an important role for model systems that allow for the rapid characterization of factor combinations.

With the appropriate stimuli in place, sprout formation and extension in our system proceeded through a well-defined progression that mirrored major steps of in vivo angiogenesis, including directed tip cell invasion, multicellular stalk formation, lumen formation, and neovessel perfusion. These steps are consistent with seminal observations of in vivo angiogenesis showing the emergence of tip cells from an existing vessel, and stalk cells that establish apical/basal polarity and form a lumen that excludes the tip cell (24, 25, 41). VEGF has been shown to be important in triggering such tip cells to extend thin, actin-rich protrusions and in guiding stalk cells to form elongated multicellular sprouts (5, 25). Here, we showed that both VEGF and S1P signaling seem to drive these filopodia-like protrusions and sprouting. Interestingly, the requirement for VEGF on sprouting depended on the composition of the angiogenic cocktail and may explain why some anti-VEGF inhibitors block angiogenesis in some instances but not others.

Many distinct mechanisms have been described for in vivo lumen formation (42). In our system, we observed fully developed lumens formed by stalk cells lining a tunnel left behind the leading tip cell. In other instances, the lumen was present only just behind the tip cell, not yet extending contiguously back to the base of the stalk, suggesting spontaneous lumen formation by the stalk cells. These observations are consistent with mechanisms for lumenization observed in vivo. Finally, in addition to the simple coordination of tip and stalk cells to form linear vessels, our system also seems to support higher-order events such as branching, a key mechanism to the patterning of sprouts controlled by the dynamic interconversion of stalk cells and filopodia-containing tip cells (25, 43–46), as well as loss of filopodial activity and regression upon eventual perfusion of the neovessel, a critical component of microvascular pruning and remodeling (47). The basis for this type of pruning could be explained by recent studies reporting that shear stress could suppress VEGF-induced invasion (37). Thus, the system introduced here faithfully recapitulates key features of in vivo angiogenesis and provides the ability to link specific stimuli to defined morphogenetic processes, further illustrating the power of such a model.

Loss-of-function in vivo models remain the mainstay for studying both physiologic and pathologic processes, including those involving angiogenesis (6, 48). However, organotypic models that are able to capture basic features of these processes in an in vitro setting undeniably offer additional levels of control and analysis that are critical to gaining mechanistic insights (15). The model system presented here highlights that the field of angiogenesis has matured sufficiently to enable reconstitution of the complex morphogenetic changes within endothelial cells as they invade to form multicellular sprouts and newly perfused vessels. Even so, it represents merely a first step toward establishing a new platform for investigating vascular remodeling. Indeed, the introduction of additional cell types, including stromal, parenchymal, and circulatory cells, could open the door to establishing a deeper understanding of how different microenvironmental, genetic, organ-specific, and pathologic factors could contribute to the different forms of angiogenesis. This study adds to recent developments (49, 50) that together highlight the importance of engineered experimental models as a new approach to studying biological processes.

Materials and Methods

Our model consists of a bilayer PDMS mold adhered to a glass coverslip (Fig. S7). Rat tail collagen type I is polymerized in the center cavity of the device around two 400-μm-diameter needles. Needle extraction leaves two cylindrical channels in the matrix. Endothelial cells are seeded into one channel and allowed to form a confluent monolayer along the wall of the cylindrical void. Devices are placed on a platform rocker to generate gravity-driven flow through both channels. Proangiogenic factors are added to the opposite channel to induce sprouting. This process is captured with brightfield or confocal microscopy. In inhibitor experiments, inhibitors were added to the system concurrently with angiogenic factors at day 0 or 3 d after sprouting was initiated. In all cases, angiogenic factors or inhibitors were refreshed daily. Detailed explanations of the materials and methods used in this study can be found in *SI Materials and Methods*.

ACKNOWLEDGMENTS. We thank Mark Breckenridge, Daniel Cohen, and Jordan Miller for technical assistance and Brendon Baker, Ritu Chaturvedi, Daniel Cohen, Jeroen Eyckmans, Jordan Miller, Sandra Ryeom, and Britta Trappmann for helpful discussions. This work was supported in part by National Institutes of Health Grants EB00262 and EB08396 and the Penn Center for Engineering Cells and Regeneration. D.-H.T.N. and S.C.S. acknowledge fellowship support from National Heart, Lung, and Blood Institute Grant HL007954 and National Cancer Institute Grant CA101871, respectively.

1. Carmeliet P (2003) Angiogenesis in health and disease. *Nat Med* 9(6):653–660.
2. Folkman J (1995) Angiogenesis in cancer, vascular, rheumatoid and other disease. *Nat Med* 1(1):27–31.
3. Witmer AN, Vrensen GF, Van Noorden CJ, Schlingemann RO (2003) Vascular endothelial growth factors and angiogenesis in eye disease. *Prog Retin Eye Res* 22(1):1–29.
4. Harmey JH, Bouchier-Hayes D (2002) Vascular endothelial growth factor (VEGF), a survival factor for tumour cells: Implications for anti-angiogenic therapy. *Bioessays* 24(3):280–283.
5. Potente M, Gerhardt H, Carmeliet P (2011) Basic and therapeutic aspects of angiogenesis. *Cell* 146(6):873–887.
6. Staton CA, Reed MW, Brown NJ (2009) A critical analysis of current in vitro and in vivo angiogenesis assays. *Int J Exp Pathol* 90(3):195–221.
7. Jain RK, Schlenger K, Höckel M, Yuan F (1997) Quantitative angiogenesis assays: Progress and problems. *Nat Med* 3(11):1203–1208.
8. Donovan D, Brown NJ, Bishop ET, Lewis CE (2001) Comparison of three in vitro human 'angiogenesis' assays with capillaries formed in vivo. *Angiogenesis* 4(2):113–121.
9. Koh W, Stratman AN, Sacharidou A, Davis GE (2008) In vitro three dimensional collagen matrix models of endothelial lumen formation during vasculogenesis and angiogenesis. *Methods Enzymol* 443:83–101.
10. Nakatsu MN, et al. (2003) Angiogenic sprouting and capillary lumen formation modeled by human umbilical vein endothelial cells (HUVEC) in fibrin gels: The role of fibroblasts and Angiopoietin-1. *Microvasc Res* 66(2):102–112.
11. Aplin AC, Fogel E, Zorzi P, Nicosia RF (2008) The aortic ring model of angiogenesis. *Methods Enzymol* 443:119–136.
12. Kang H, Bayless KJ, Kaunas R (2008) Fluid shear stress modulates endothelial cell invasion into three-dimensional collagen matrices. *Am J Physiol Heart Circ Physiol* 295(5):H2087–H2097.
13. Meier F, et al. (2000) Human melanoma progression in skin reconstructs : Biological significance of bFGF. *Am J Pathol* 156(1):193–200.
14. Debnath J, Brugge JS (2005) Modelling glandular epithelial cancers in three-dimensional cultures. *Nat Rev Cancer* 5(9):675–688.
15. Schmeichel KL, Bissell MJ (2003) Modeling tissue-specific signaling and organ function in three dimensions. *J Cell Sci* 116(Pt 12):2377–2388.
16. Montesano R, Vassalli JD, Baird A, Guillemin R, Orci L (1986) Basic fibroblast growth factor induces angiogenesis in vitro. *Proc Natl Acad Sci USA* 83(19):7297–7301.
17. Silvagno F, et al. (1995) In vivo activation of met tyrosine kinase by heterodimeric hepatocyte growth factor molecule promotes angiogenesis. *Arterioscler Thromb Vasc Biol* 15(11):1857–1865.
18. Fong GH, Rossant J, Gertsenstein M, Breitman ML (1995) Role of the Flt-1 receptor tyrosine kinase in regulating the assembly of vascular endothelium. *Nature* 376(6535):66–70.
19. Carmeliet P, et al. (1996) Abnormal blood vessel development and lethality in embryos lacking a single VEGF allele. *Nature* 380(6573):435–439.
20. Salcedo R, et al. (2000) Human endothelial cells express CCR2 and respond to MCP-1: direct role of MCP-1 in angiogenesis and tumor progression. *Blood* 96(1):34–40.
21. Kono M, et al. (2004) The sphingosine-1-phosphate receptors S1P1, S1P2, and S1P3 function coordinately during embryonic angiogenesis. *J Biol Chem* 279(28):29367–29373.
22. Bayless KJ, Davis GE (2003) Sphingosine-1-phosphate markedly induces matrix metalloproteinase and integrin-dependent human endothelial cell invasion and lumen formation in three-dimensional collagen and fibrin matrices. *Biochem Biophys Res Commun* 312(4):903–913.
23. Montesano R, Orci L (1985) Tumor-promoting phorbol esters induce angiogenesis in vitro. *Cell* 42(2):469–477.
24. Lampugnani MG, et al. (2010) CCM1 regulates vascular-lumen organization by inducing endothelial polarity. *J Cell Sci* 123(Pt 7):1073–1080.
25. Gerhardt H, et al. (2003) VEGF guides angiogenic sprouting utilizing endothelial tip cell filopodia. *J Cell Biol* 161(6):1163–1177.
26. Mendel DB, et al. (2000) Development of SU5416, a selective small molecule inhibitor of VEGF receptor tyrosine kinase activity, as an anti-angiogenesis agent. *Anticancer Drug Des* 15(1):29–41.
27. Mendel DB, et al. (2000) The angiogenesis inhibitor SU5416 has long-lasting effects on vascular endothelial growth factor receptor phosphorylation and function. *Clin Cancer Res* 6(12):4848–4858.
28. Inai T, et al. (2004) Inhibition of vascular endothelial growth factor (VEGF) signaling in cancer causes loss of endothelial fenestrations, regression of tumor vessels, and appearance of basement membrane ghosts. *Am J Pathol* 165(1):35–52.
29. Lee OH, et al. (1999) Sphingosine 1-phosphate induces angiogenesis: Its angiogenic action and signaling mechanism in human umbilical vein endothelial cells. *Biochem Biophys Res Commun* 264(3):743–750.
30. LaMontagne K, et al. (2006) Antagonism of sphingosine-1-phosphate receptors by FTY720 inhibits angiogenesis and tumor vascularization. *Cancer Res* 66(1):221–231.
31. Brown PD (1997) Matrix metalloproteinase inhibitors in the treatment of cancer. *Med Oncol* 14(1):1–10.
32. Steward WP, Thomas AL (2000) Marimastat: The clinical development of a matrix metalloproteinase inhibitor. *Expert Opin Investig Drugs* 9(12):2913–2922.
33. Chrobak KM, Potter DR, Tien J (2006) Formation of perfused, functional microvascular tubes in vitro. *Microvasc Res* 71(3):185–196.
34. Miller JS, et al. (2012) Rapid casting of patterned vascular networks for perfusable engineered three-dimensional tissues. *Nat Mater* 11(9):768–774.
35. Zheng Y, et al. (2012) In vitro microvessels for the study of angiogenesis and thrombosis. *Proc Natl Acad Sci USA* 109(24):9342–9347.
36. Chung S, et al. (2009) Cell migration into scaffolds under co-culture conditions in a microfluidic platform. *Lab Chip* 9(2):269–275.
37. Song JW, Munn LL (2011) Fluid forces control endothelial sprouting. *Proc Natl Acad Sci USA* 108(37):15342–15347.
38. Yeon JH, Ryu HR, Chung M, Hu QP, Jeon NL (2012) In vitro formation and characterization of a perfusable three-dimensional tubular capillary network in microfluidic devices. *Lab Chip* 12(16):2815–2822.
39. Newman AC, Nakatsu MN, Chou W, Gershon PD, Hughes CC (2011) The requirement for fibroblasts in angiogenesis: Fibroblast-derived matrix proteins are essential for endothelial cell lumen formation. *Mol Biol Cell* 22(20):3791–3800.
40. Stratman AN, Davis MJ, Davis GE (2011) VEGF and FGF prime vascular tube morphogenesis and sprouting directed by hematopoietic stem cell cytokines. *Blood* 117(14):3709–3719.
41. Holderfield MT, Hughes CC (2008) Crosstalk between vascular endothelial growth factor, notch, and transforming growth factor-beta in vascular morphogenesis. *Circ Res* 102(6):637–652.
42. Iruela-Arispe ML, Davis GE (2009) Cellular and molecular mechanisms of vascular lumen formation. *Dev Cell* 16(2):222–231.
43. Eilken HM, Adams RH (2010) Dynamics of endothelial cell behavior in sprouting angiogenesis. *Curr Opin Cell Biol* 22(5):617–625.
44. Carmeliet P, De Smet F, Loges S, Mazzone M (2009) Branching morphogenesis and antiangiogenesis candidates: Tip cells lead the way. *Nat Rev Clin Oncol* 6(6):315–326.
45. Hellström M, et al. (2007) Dll4 signalling through Notch1 regulates formation of tip cells during angiogenesis. *Nature* 445(7129):776–780.
46. Suchting S, et al. (2007) The Notch ligand Delta-like 4 negatively regulates endothelial tip cell formation and vessel branching. *Proc Natl Acad Sci USA* 104(9):3225–3230.
47. le Noble F, et al. (2005) Control of arterial branching morphogenesis in embryogenesis: go with the flow. *Cardiovasc Res* 65(3):619–628.
48. Hasan J, et al. (2004) Quantitative angiogenesis assays in vivo—A review. *Angiogenesis* 7(1):1–16.
49. Huh D, et al. (2010) Reconstituting organ-level lung functions on a chip. *Science* 328(5986):1662–1668.
50. Barrila J, et al. (2010) Organotypic 3D cell culture models: Using the rotating wall vessel to study host-pathogen interactions. *Nat Rev Microbiol* 8(11):791–801.

Supporting Information

Nguyen et al. 10.1073/pnas.1221526110

SI Materials and Methods

Device Fabrication. The device housing is fabricated from two patterned layers of poly(dimethylsiloxane) (PDMS; Sylgard 184; Dow-Corning) bonded to each other and sealed against a glass substrate (Fig. S7). The two PDMS layers were cast or double-cast from templates originally generated using standard photolithography of SU-8 on silicon wafers. Dimensions of important features in both layers are shown in Fig. 1*A*. To assemble the device, the bottom layer was first sealed to a glass coverslip. The top and bottom layers were then treated with oxygen plasma, bonded together, and cured at 110 °C overnight. Assembled devices then were treated with oxygen plasma, immersed in 0.1 mg/mL poly-L-lysine (Sigma) for 1 h, 1% glutaraldehyde (Sigma) for 1.5 h, washed several times with double-distilled H_2O, sterilized with UV light for 15 min, and soaked in 70% (vol/vol) ethanol for 1 h. To mold cylindrical channels, two 400-μm-diameter acupuncture needles (Hwato) were inserted into parallel grooves at the top of the bottom layer (Fig. S7) and through the middle rectangular chamber ∼200 μm above the glass coverslip surface. Rat tail collagen type I (2.5 mg/mL; BD Biosciences) was prepared per the manufacturer's protocol and pipetted into the middle chamber and allowed to polymerize at 37 °C for 30 min. Excess collagen was subsequently aspirated from the fluid reservoirs feeding from the middle chamber. Devices were then covered with EGM-2 (Lonza) before the needles were extracted as previously described (1).

Cell Culture and Seeding in Devices. Human umbilical vein endothelial cells (HUVECs) (Lonza) and human microvascular endothelial cells (HMVECs) (Lonza) were cultured in endothelial cell growth medium EGM-2 and EGM-2MV, respectively. Although all experiments shown were conducted with HUVECs, HMVECs also sprouted in response to angiogenic cocktails. Endothelial cells (ECs) were concentrated at 10^7 cells/mL and seeded into one of the two channels. The device was inverted to allow ECs to adhere to the top surface of the channel for 10 min and then flipped upright to allow cells to adhere to the bottom surface of the channel for another 10 min. Cells that adhered in the fluid reservoirs were scraped off with a pipette tip, and unattached cells in the channel were thoroughly flushed out with PBS. Media was immediately added thereafter and the devices were placed on a platform rocker (BenchRocker BR2000). Cells were cultured in channels for 1–2 d before angiogenic factors were introduced.

Immunofluorescence Staining. For immunofluorescence staining, cells in the devices were fixed in situ with 3.7% (wt/wt) formaldehyde for 45 min. For CD31 labeling, cells were permeabilized with 0.1% Triton-X for 30 min, blocked in 3% (wt/wt) BSA overnight at 4 °C, washed three times with PBS, and incubated with mouse monoclonal antibody against human CD31 (1:200; Dako). For laminin, collagen IV, and podocalyxin labeling, samples were blocked with 3% (wt/wt) BSA overnight at 4 °C, washed three times with PBS, and incubated at 4 °C overnight with rabbit polyclonal antibody against laminin (1:100; Chemicon), mouse polyclonal antibody against collagen IV (1:50; Dako), and goat polyclonal anti-human podocalyxin (1:100; R&D), respectively. Before secondary antibody incubation, the devices were washed overnight with PBS at 4 °C. All secondary antibodies (Invitrogen) were used at 1:500 dilution. Cell nuclei were labeled with DAPI (1:500; Sigma). F-actin was labeled with Alexa Fluor 488-conjugated phalloidin (1:100; Sigma).

Image Acquisition and Processing. Brightfield images of sprouts were acquired with a Nikon TE200 epifluorescence microscope (Nikon Instruments, Inc.) using a 10× objective. Confocal immunofluorescence images were acquired with either a 10× air objective or an LD C-Apochromat 40×, 1.1 N.A. water-immersion objective attached to either an Axiovert 200M inverted microscope (Zeiss) equipped with a CSU10 spinning disk confocal scan head (Yokogawa Electric Corp.) and an Evolve EMCCD camera (Photometrics) or an Olympus IX 81 microscope (Olympus America, Inc.) equipped with an CSU-X1 spinning disk confocal scan head (Yokogawa Electric Corp.) and an Andor iXon3 897 EMCCD camera (Andor Technology). ImageJ was used to merge channels, perform z-projection for all confocal stacks, and generate longitudinal and transverse cross-sections. Custom MATLAB scripts and ImageJ were used to stitch images together.

Treatment with Pro- and Antiangiogenic Factors. In screening experiments, the endothelialized parent vessel was perfused with culture media and the source channel was perfused with media enriched with angiogenic factors. Angiogenic factors include VEGF, monocyte chemotactic protein-1 (MCP-1), hepatocyte growth factor (HGF), and basic fibroblast growth factor (bFGF), all purchased from R&D Systems. Sphingosine-1-phosphate (S1P) and phorbol myristate acetate (PMA) were purchased from Cayman Chemical and Sigma, respectively. VEGF, MCP-1, bFGF, HGF, and PMA were all used at 75 ng/mL; S1P was used at 500 nM unless otherwise indicated. Inhibitors targeting VEGF receptor 2 (10 μM Semaxanib; Cayman Chemical) or S1P receptors (100 nM Fingolimod; Selleck Chemicals) were administered into both channels. Matrix metalloproteinase (MMP) inhibitor (0.6 μM Marimastat; Tocris Bioscience) was administered into the source channel. Media in both channels were refreshed daily.

Bead Perfusion of Microvessels. After neovessels bridged the two preformed channels in the device, a solution of CellTracker CM-DiI (Invitrogen) was delivered into the parent vessel to label cells in situ. Fluorescent beads (Polysciences) of 3-μm diameter were suspended in PBS and perfused into the parent vessel at a flow rate of 5 μL/min. Images were acquired at 40 frames/s using an Eclipse TE2000 equipped with an Evolve EMCCD camera.

Quantification of Sprout Length and Sprout Density. Custom MATLAB code was written to measure the individual distances from the leading protrusions of tip cells to the wall of the parent vessel. Tip cells were additionally quantified as either attached to stalk cells extending from the endothelialized channel or as isolated single cells (Fig. S2). Sprouting metrics were quantified for the screening experiment ($n = 2$ samples per condition), the VEGFR2 and S1P inhibitor experiment ($n = 5$ samples per condition), and the MMPs inhibitor experiment ($n = 3$ samples per condition).

Filopodia Quantification and Analysis. Projections from z-resolved confocal stacks, which were taken with a 25× objective, Axiovert 200M inverted microscope (Zeiss), and spinning disk confocal scan head, were used to analyze filopodia length and number. A custom MATLAB code was used to determine the distance from the tips of filopodia to the nearest edge of the cell body and to count the number of filopodia. The number and length of filopodia were averaged over the number of cells across three samples per condition.

Characterization of Gradient. Twenty-kilodalton fluorescein isothiocyanate–dextran (Sigma) was perfused into the source channel and the fluorescence signal across the interstitial space between the parent endothelialized vessel and the source channel was recorded for 1 h using an Axiovert 200M inverted microscope

equipped with an 40× water-immersion objective, CSU10 spinning disk confocal scan head, and an Evolve EMCCD camera. Intensity was normalized to maximum intensity and plotted over the distance between the source and sink channels.

Statistical Analysis. Sample populations were compared using unpaired, two-tailed Student t test. $P < 0.05$ was the threshold for statistical significance. Data points on the graphs represent mean values and error bars depict SEM.

1. Chrobak KM, Potter DR, Tien J (2006) Formation of perfused, functional microvascular tubes in vitro. *Microvasc Res* 71(3):185–196.

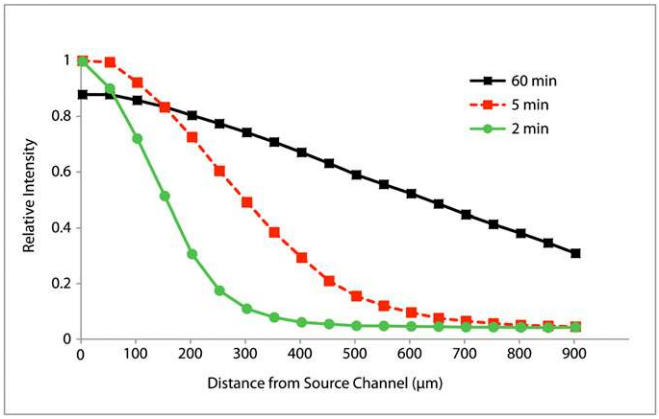

Fig. S1. Characterization of gradient between parent vessel and source channel. Relative intensity profiles at 2, 5, and 60 min after addition of 20-kDa fluorescently tagged dextran. A 1D solution to Fick's Law using data acquired at 2 min after introduction of the dextran provided an estimate for the diffusion coefficient of 1.80×10^{-6} cm^2/s.

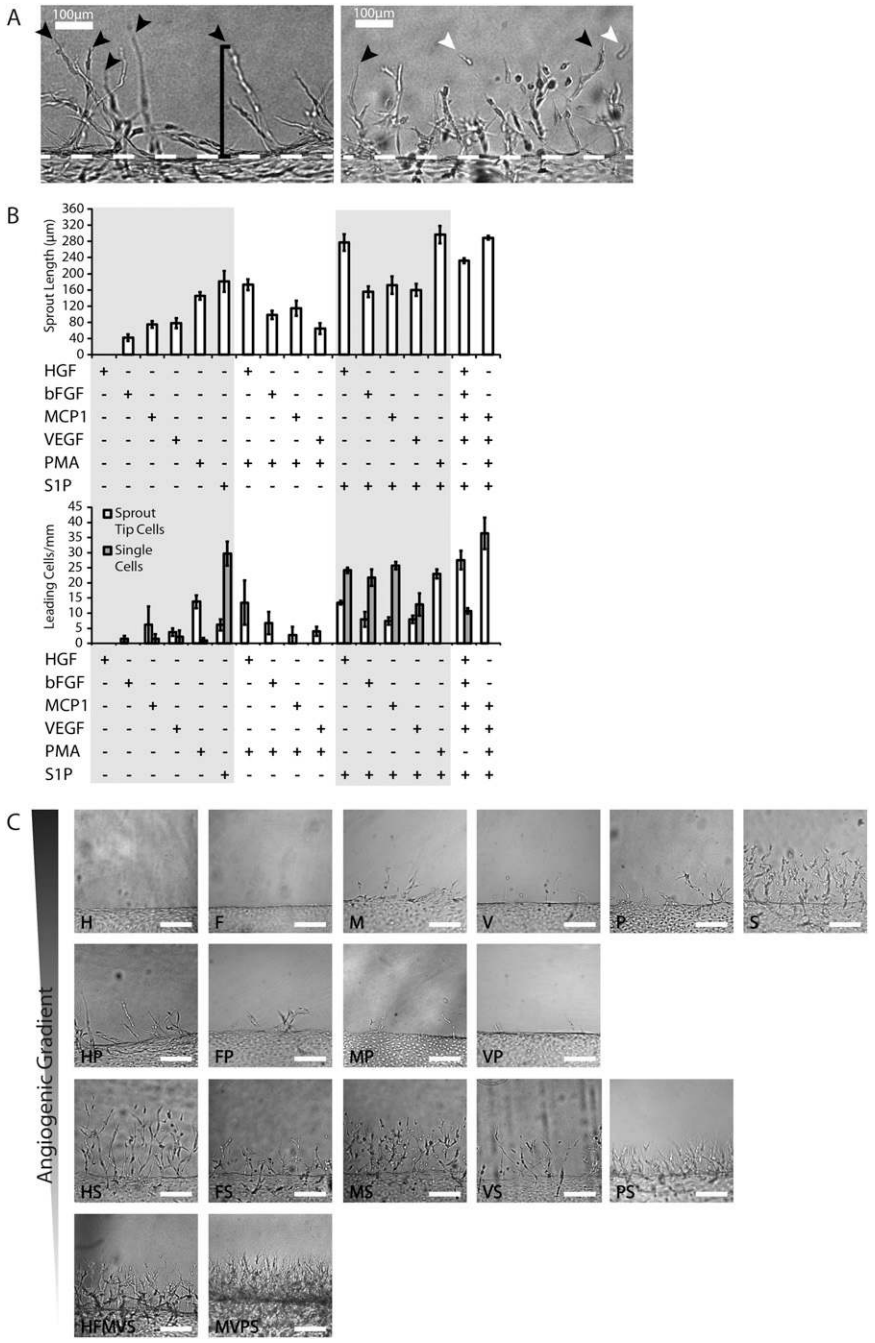

Fig. S2. Quantitative metrics for scoring number and length of sprouts and single cell migration. (*A*) Leading cells are categorized as sprout tip cells (black arrowheads) when in contact with stalk cells that are connected to the parent vessel (dashed white line) or as isolated, single cells (white arrowheads). Sprout length was measured as the distance between leading protrusions of sprout tip cells and the nearest point along the parent vessel. (Scale bars: 100 μm.) (*B*) Plot of sprout length and the number of sprout tip cells and single cells after 4 d of exposure to indicated factor(s). $n = 2$ samples per condition. (*C*) Representative phase images of each condition after 4 d of exposure to indicated factor(s). (Scale bars: 200 μm.) F, bFGF; H, HGF; M, MCP-1; P, PMA; S, S1P; V, VEGF.

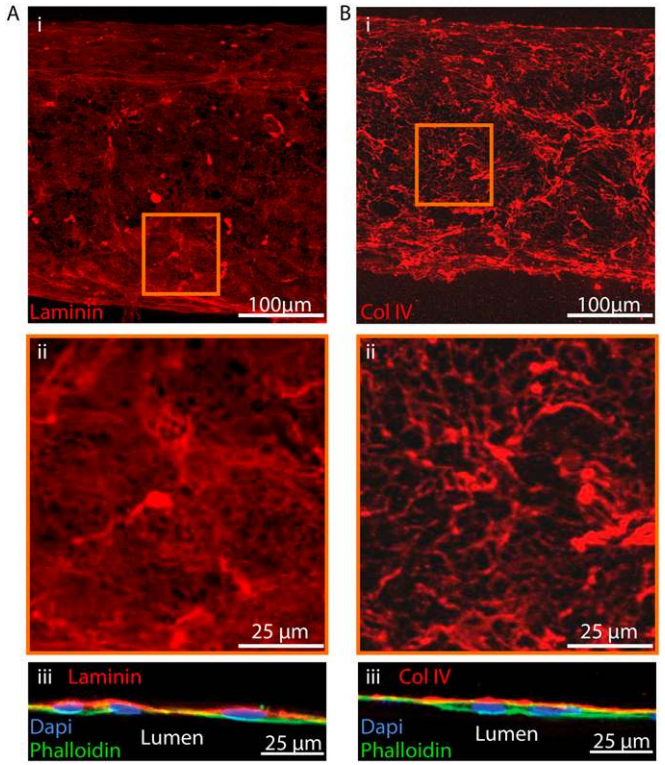

Fig. S3. Characterization of cell-deposited extracellular matrices by the endothelium. (*A*) Laminin immunofluorescence (red) is shown in a z-resolved confocal stack en face projection of a parent vessel (*i*), with zoomed-in view (*ii*). Radial slice (*iii*) indicating localization of laminin at the basal side. (*B*) Collagen IV immunofluorescence (red) is shown in a z-resolved confocal stack projection of a parent vessel (*i*), with zoomed-in view (*ii*). Radial slice (*iii*) indicating localization of collagen IV at the basal side. F-actin and nuclei are labeled with phalloidin (green) and DAPI (blue).

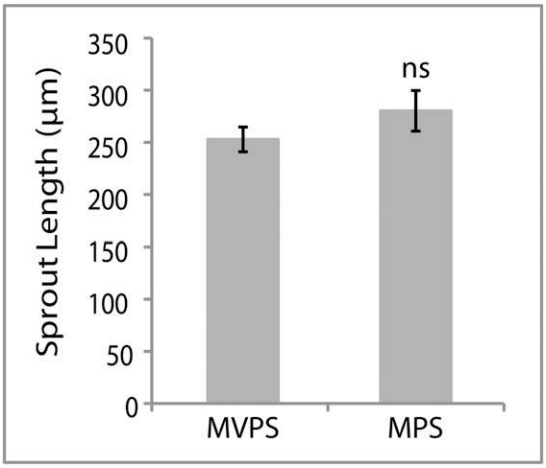

Fig. S4. Quantification of sprout length for the MVPS and MPS cocktails at day 4. MVPS and MPS cocktails were only added to the source channel. Error bars are SEM. ns, no significant difference from MVPS control ($P \geq 0.05$).

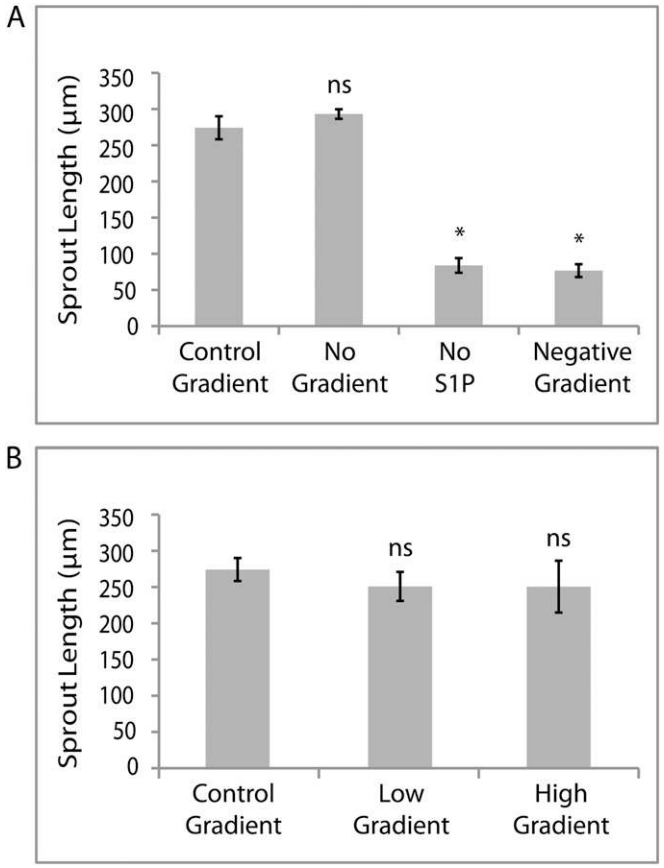

Fig. S5. Quantification of sprout length for different S1P gradients. (*A*) Plot of sprout length at day 4 for the MVPS cocktail in source channel (control gradient), MVPS in source channel plus S1P in parent vessel (no gradient), MVP in source channel plus S1P in parent channel (negative gradient), and MVP in source channel (no S1P). (*B*) Plot of sprout length at day 4 for the MVPS cocktail in source channel with different concentrations of S1P: 250 nM (low gradient), 500 nM (control gradient) and 1 μM (high gradient). *Significant difference from the MVPS (control gradient) ($P < 0.05$); ns, no significant difference from MVPS (control gradient) control.

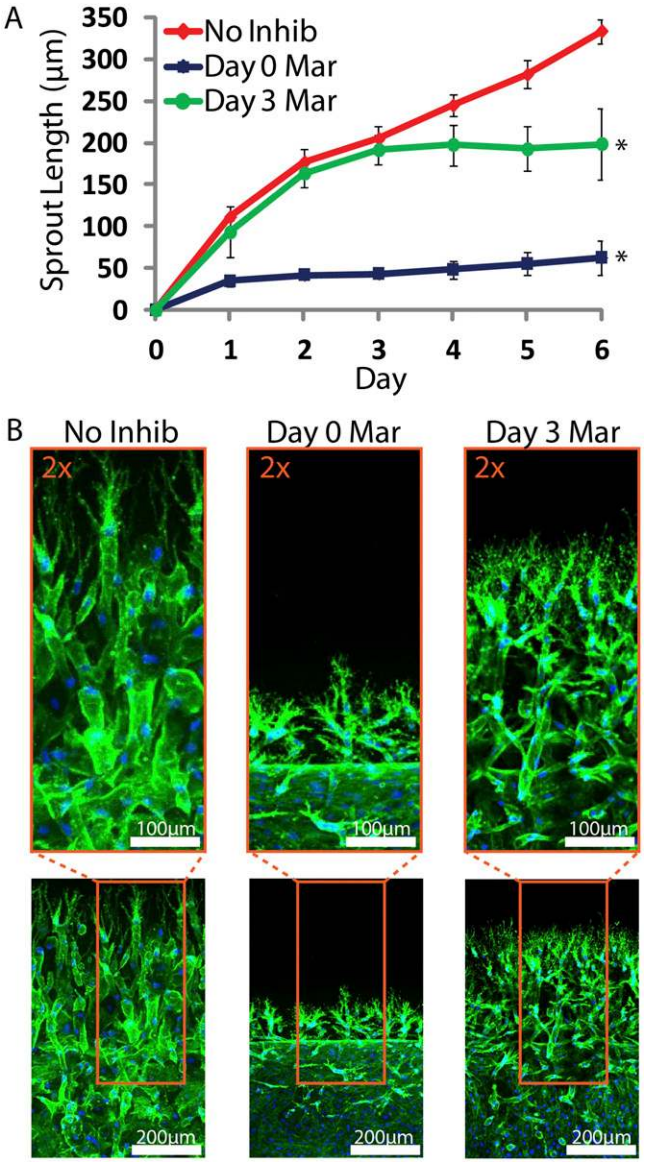

Fig. S6. Effects of MMP inhibition on angiogenic sprouting. (*A*) Plot of sprout length driven by MVPS in response to Marimastat treatment over time. Proangiogenic cocktail was initiated at day 0 and Marimastat treatment was initiated at either day 0 (Day 0 Mar), day 3 (Day 3 Mar), or never (No Inhib). Error bars are SEM. *Significant difference from control ($P < 0.05$). $n = 3$ samples for sprout length quantification. (*B*) Representative confocal immunofluorescence images of indicated conditions at day 6. F-actin and nuclei are labeled with phalloidin (green) and DAPI (blue), respectively.

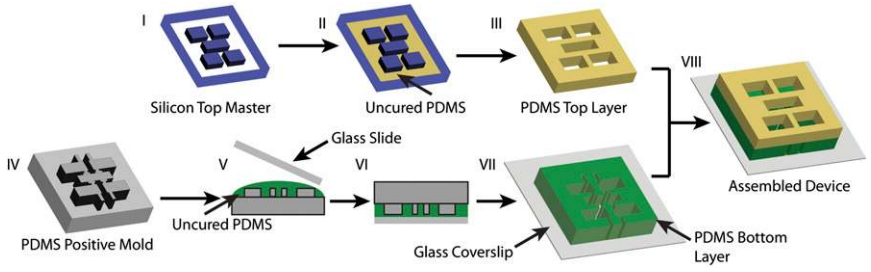

Fig. S7. Schematic of the device manufacturing process. A silicon template (blue and white) containing four rectangular features for the top layer of the device was made using UV lithography (*I*). Uncured PDMS (beige) was cast onto silicon template (*II*). After curing at 80 °C, PDMS top layer (beige) was cast off the template (*III*). A silicon template containing four linked rectangular features was used to make a bottom positive PDMS mold (gray) (*IV*). Uncured PDMS (green) was cast onto positive PDMS mold and a glass slide was applied to trap the PDMS between the mold and glass (*V*). System was inverted (*VI*). After curing at 110 °C, PDMS bottom layer (green) was cast off the PDMS mold and adhered to a glass coverslip (*VII*). Following oxygen plasma treatment, top and bottom PDMS layers were aligned and sealed and placed in a 110 °C oven overnight.

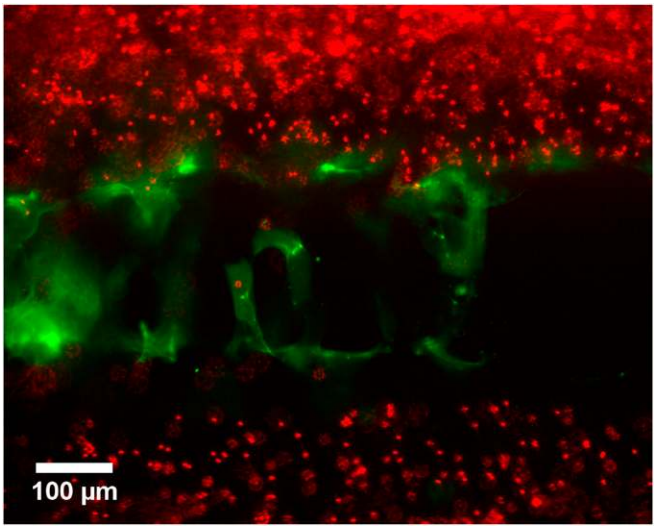

Movie S1. Three-micrometer fluorescent beads (red) were perfused into the parent vessel at a flow rate of 5 μL/min. Beads flowed through lumen of the neovessels to the source channel. Endothelial cells (green) were stained with DiI. Images were acquired at 40 frames/s. Movie length is ~5 s.

Movie S1